PROCEEDINGS OF THE ROYAL SOCIETY A MATHEMATICAL, PHYSICAL & ENGINEERING SCIENCES

Nonlinear Poisson effects in soft honeycombs

L. Angela Mihai and Alain Goriely

Proc. R. Soc. A 2014 **470**, 20140363, published 16 July 2014

PROCEEDINGS OF THE ROYAL SOCIETY A

rspa.royalsocietypublishing.org

Research

Cite this article: Mihai LA, Goriely A. 2014 Nonlinear Poisson effects in soft honeycombs. *Proc. R. Soc. A* **470**: 20140363.
http://dx.doi.org/10.1098/rspa.2014.0363

Received: 4 May 2014
Accepted: 16 June 2014

Subject Areas:
applied mathematics, mathematical modelling

Keywords:
constitutive behaviour, cellular structures, elastic material, large strain, finite elements

Author for correspondence:
L. Angela Mihai
e-mail: MihaiLA@cardiff.ax.uk

Royal Society Publishing

Nonlinear Poisson effects in soft honeycombs

L. Angela Mihai[1] and Alain Goriely[2]

[1]School of Mathematics, Cardiff University, Senghennydd Road, Cardiff CF24 4AG, UK
[2]Mathematical Institute, University of Oxford, Woodstock Road, Oxford OX2 6GG, UK

LAM, 0000-0003-0863-3729; AG, 0000-0002-6436-8483

We examine solid cellular structures within the theoretical framework of finite elasticity, whereby we assume that the cell wall material is nonlinear elastic. This enables us to identify new mechanical effects that appear in cellular materials when elastically deformed, and to explore the physical properties that influence them. We find that, when a honeycomb structure of hyperelastic material and standard geometry, such as rectangular-, hexagonal- or diamond-shaped cells, contains walls which are inclined relative to an applied uniaxial tensile load, these walls tend to expand both in the direction of the load and in the perpendicular direction, producing an apparent negative Poisson's ratio at local cell level. Moreover, we show that this (negative) Poisson ratio decreases as the magnitude of the tensile load increases. For these structures, Poisson's ratios greater than 0.5 are obtained in uniaxial compression. Similar effects in structures with linearly elastic cell walls do not occur.

1. Introduction

Solid cellular structures are widespread in nature and industry, from marine sponges and plant stems, which have been around for million of years, to biomedical tissue scaffolds and synthetic foams, which are under continuous research and development [1,2]. Apparently, Galileo Galilei (1564–1642) suggested that bones must contain voids to account for their high strength-to-weight ratio, and also observed that bones of a large animal need to be thicker in proportion to their size than those of smaller animals, whereas Robert Hooke (1635–1703) introduced the word 'cell' to describe the microscopic structure of cork, as well as the law 'ut tensio sic vis', i.e. 'as the extension, so the force' [3].

At low stresses or strains, the assumption that the cell walls are linearly elastic with a geometrically nonlinear behaviour is valid, and is successfully used in structural mechanics and other engineering applications (e.g. metal foams) [4]. However, many modern applications and biological structures involve large strains, where the deformation is inherently nonlinear and the corresponding stresses depend on both the position and the underlying material properties. For these complex materials to be understood and optimized with respect to their mechanical response, reliable computer models supported by mathematical and mechanical analysis are needed [5].

In this study, we examine solid cellular structures within the theoretical framework of finite elasticity, whereby we assume that *the cell wall material is nonlinear elastic* [6,7]. This enables us to identify new mechanical effects that appear in cellular materials when elastically deformed, and to explore the physical properties that influence them. We find that, for soft honeycomb structures with hyperelastic walls and standard geometry, such as rectangular-, hexagonal- or diamond-shaped cells, non-standard Poisson effects arise from the combination of nonlinear elastic responses and structural geometry.

First, we present a set of numerical models for periodic honeycomb structures of nonlinear hyperelastic material with a small number of cells, and report on their elastic behaviour when subjected to external tensile or compressive forces (§2). For a honeycomb structure, which is either extended or compressed in one direction to a certain strain E_1, and is unconstrained in the orthogonal direction, there is a strain E_2 generated in that direction. Then, for this deformation, an (apparent) Poisson's ratio can be defined as the negative quotient of the second to the first strain, $\nu = -E_2/E_1$. Although, in practice, Poisson's ratios are more often computed for small strains, this definition also applies in the case of large strains. However, while in the small strain regime, the Poisson's ratio is always a constant, in the finite strain case, this ratio may be a non-constant function of the deformation [8]. In finite elasticity also, uniaxial tensile loading leads to a simple extension in the direction of the (positive) tensile force, whereby the ratio between the tensile strain, and the strain in the orthogonal direction is greater than one, if and only if the Baker–Ericksen inequalities hold [9,10]. Moreover, non-uniqueness of deformation is possible under external tensile conditions, where different apparent Poisson's ratios may be computed [11]. If the material is anisotropic (e.g. foams), then different Poisson's ratios may also be found as the material is extended (or compressed) in different directions. Even for transversely isotropic materials, if the orientation of the axis of isotropy does not coincide with the orientation of the applied load, then a simple tension does not produce a simple extension, and the analysis is more involved.

As the deformation of cellular bodies under external loading is typically non-homogeneous, owing to both the cell wall material and the individual cell geometry, here we limit our investigation to the apparent Poisson effect that may be defined in terms of the large strain components generated in the cell walls under specific tensile or compressive conditions. Then, for the nonlinear elastic cell walls, we express the Poisson's ratio either in terms of the logarithmic (true) or the Green–Lagrange strain components, and exploit the fact that the sign and the monotonicity of the computed Poisson function is independent of which of these two strains is chosen. In the linear elastic limit, the logarithmic and the Green–Lagrange strains are both equal to the infinitesimal strain tensor. For the model structures, we find that Poisson's ratios that are either negative or greater than 0.5 can be obtained when large strain deformations of the cell walls are permitted.

We note that negative Poisson's ratios were reported in cork under non-radial (axial or transverse) compression [12], whereas Poisson's ratios with values between 0.6 and 0.8 were measured in some woods where the primary strain was extensional in the radial direction, and the secondary strain was compressive in the transverse direction [13, p. 82]. A Poisson's ratio equal to 1 was also computed for hexagonal cells under the small strain assumption [2, p. 119].

Motivated by our numerical results, we then focus on the mechanical treatment of a single oblique wall, and show that the Poisson effects observed in these structures are influenced by the inclination of the cell wall relative to the direction of the applied load (§3). Specifically, for a

structure of nonlinear elastic material which is extended vertically, by computing the (apparent) Poisson's ratio generated in the elastic walls as the negative quotient of the horizontal to the vertical true strain component, we find that the oblique walls extend both in the direction of the applied load and in the transverse direction, causing a negative Poisson effect. Because this effect is not observed when the elasticity of the cell wall material is linear, we infer that the richer mechanical behaviour observed here is due to the inextricable relation between the nonlinear elastic responses and the structural architecture of honeycombs with softer cell walls.

2. The elastic qualities of soft honeycombs

We begin our investigation with a set of numerical examples that illustrate the mechanical performance of honeycomb structure with nonlinear hyperelastic cell walls. Hyperelastic (or Green elastic) materials are the class of material models described by a strain energy function. For these models, boundary value problems may be cast as variational problems, which then can be used to generate finite-element methods [14,15]. The computational examples here recorded were produced within the open-source software finite elements for biomechanics environment [16]. The four different model structures that we consider are depicted, in their undeformed state, in figure 1. In figure 1, every structure is made from a single piece of material and occupies a thin square domain of side one in the horizontal and vertical direction. The cells in each structure are equal in size and are uniformly distributed throughout the structure, whereas their specific geometries are as follows: (i) square shapes in stacked cell distribution, (ii) squares in staggered distribution, (iii) diamonds (rhombus shapes) and (iv) hexagons. In the graphical illustrations, the cell diameter is approximately $\frac{1}{7}$, and the finite-element mesh for the numerical discretization of the elastic cell walls is also shown. While these specifications are required for the numerical implementation, the subsequent qualitative analysis remains valid if other cell and mesh sizes are considered.

For the honeycomb models, the cell wall material is characterized by the following strain energy function:

$$\mathcal{W}(I_1, I_2, I_3) = \frac{\mu_1}{2}(I_3^{-1/3} I_1 - 3) + \frac{\mu_2}{2}(I_3^{-2/3} I_2 - 3) + \frac{\kappa}{2}(I_3^{1/2} - 1)^2, \tag{2.1}$$

where μ_1, μ_2, κ are constants, such that $\mu = \mu_1 + \mu_2 > 0$ and $\kappa > 0$, and

$$I_1(\mathbf{B}) = \operatorname{tr} \mathbf{B}, \quad I_2(\mathbf{B}) = \tfrac{1}{2}((\operatorname{tr} \mathbf{B})^2 - \operatorname{tr} \mathbf{B}^2), \quad I_3(\mathbf{B}) = \det \mathbf{B}$$

represent the principal invariants of the left Cauchy–Green strain tensor $\mathbf{B}$. In the incompressible case ($I_3 = 1$), the material is described by the classical Mooney–Rivlin model.

The corresponding Cauchy stress in the cell walls has the Rivlin–Ericksen representation [9]:

$$\boldsymbol{\sigma} = \beta_0 \mathbf{I} + \beta_1 \mathbf{B} + \beta_{-1} \mathbf{B}^{-1}, \tag{2.2}$$

where

$$\beta_0 = \frac{2}{\sqrt{I_3}}\left(I_2 \frac{\partial \mathcal{W}}{\partial I_2} + I_3 \frac{\partial \mathcal{W}}{\partial I_3}\right), \quad \beta_1 = \frac{2}{\sqrt{I_3}} \frac{\partial \mathcal{W}}{\partial I_1} \quad \text{and} \quad \beta_{-1} = -2\sqrt{I_3} \frac{\partial \mathcal{W}}{\partial I_2}.$$

If the material is incompressible, then the representation (2.2) is replaced by the form

$$\boldsymbol{\sigma} = -p\mathbf{I} + \beta_1 \mathbf{B} + \beta_{-1} \mathbf{B}^{-1},$$

where p denotes an arbitrary hydrostatic pressure.

Setting the constitutive parameters as $\mu_1 = 1.2$, $\mu_2 = 0.2$ and $\kappa = 100$ MPa, we submit the model structures to either vertical extension or compression as follows: the lower external horizontal faces are fixed in all three directions, the upper external horizontal faces are subjected to a prescribed vertical displacement and are fixed in the other two directions, whereas the remaining internal and external faces of the cell walls may deform freely. The resulting deformations in the honeycomb models are shown in figures 2, 3, 7 and 8.

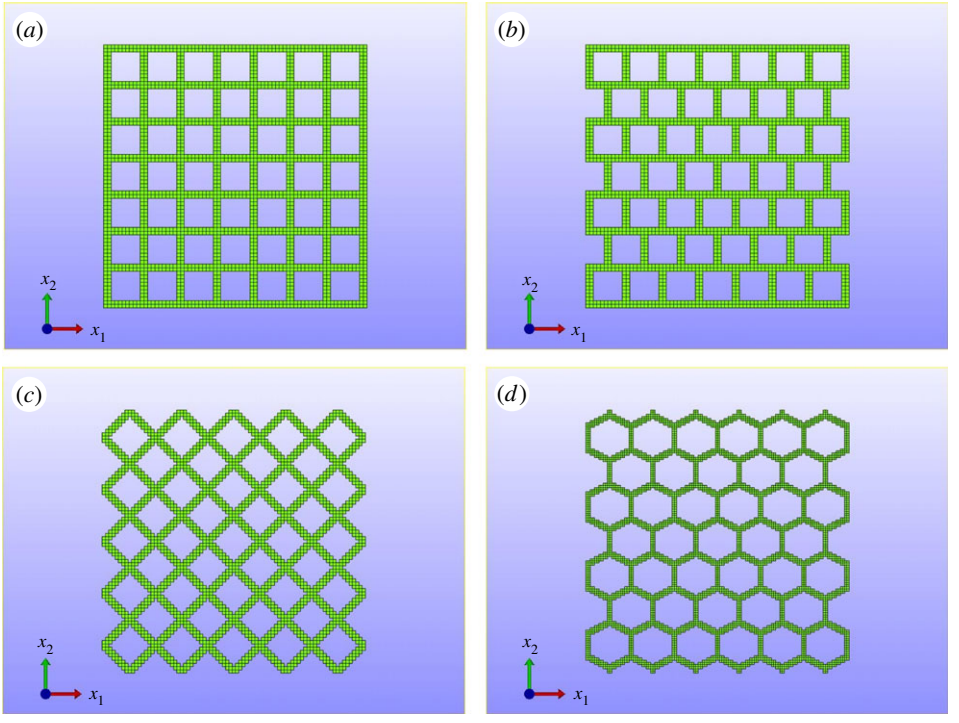

Figure 1. Undeformed honeycombs with (*a*) stacked square, (*b*) staggered square, (*c*) diamond and (*d*) hexagonal cell geometry, occupying a total square domain of side one. (Online version in colour.)

When a *large vertical tension* is applied, figures 2 and 3 indicate that, for every structure, the deformation is always symmetric with respect to the vertical axis. The corresponding maximum horizontal and vertical displacements are recorded by the diagrams in figure 4*a*, from which we infer that the transverse (secondary) displacement is generally much smaller than the axial (primary) displacement. From these diagrams, we also deduce that the structure with staggered square cells contracts less in the transverse direction than the other structures, whereas that with diamond-shaped cells contracts the most. Moreover, as the staggered square cells tend to deform into hexagonal shapes under vertical extension, whereas the hexagonal cells deform into nearly rectangular shapes under horizontal extension, these geometrical changes are captured also by the corresponding diagrams associated with the staggered and hexagonal cells, respectively, which intersect each other at sufficiently large displacements.

We then compute *the apparent Poisson's ratio* in the elastic material throughout the structure as the negative quotient of the average value of the horizontal to the vertical component of the logarithmic strain $\ln \mathbf{C}^{1/2}$, where $\mathbf{C}$ is the right Cauchy–Green strain tensor, and the logarithmic function is applied component-wise. The average values are calculated by summing the values for all the finite elements in the model and dividing by the number of elements. Figure 5*a* shows that, for the honeycomb structures, these Poisson's ratios are smaller than for the underlying compact material, and decrease as the deformation increases, and may become zero or negative in structures with staggered, diamond or hexagonal cells. This is an interesting phenomenon, which is not observed under the small strain regime. In addition, the Poisson's ratio is smaller for the diamond cells structure than for the structure with hexagonal cells, whereas for the structure with staggered square cells, this is closer to that of the underlying material, which in this case is nearly 0.5. A comparison with the results for the relative displacements in figure 4*a* then suggests that the larger the horizontal displacement the lower the Poisson's ratio found in a structure. *This is an important observation that will enable us to carry out an analytical investigation of the cause for the observed Poisson effects in the next section.*

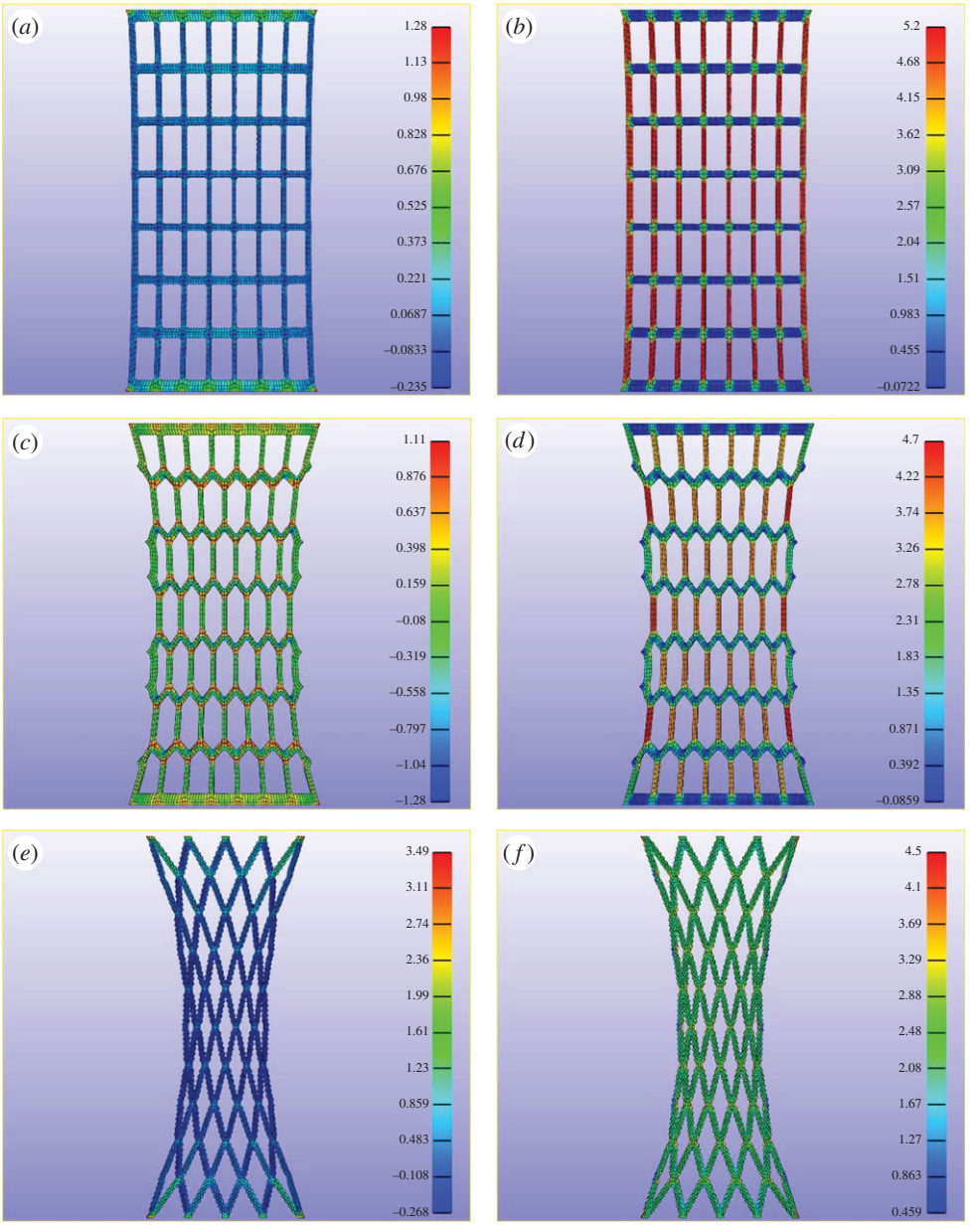

Figure 2. Vertical extension owing to prescribed vertical displacement equal to 1 at the top external boundary, showing (*a*,*c*,*e*) horizontal and (*b*,*d*,*f*) vertical stresses in honeycombs with stacked, staggered and diamond cells, respectively. (Online version in colour.)

In finite elasticity, a Poisson's ratio can also be computed as the negative quotient of the horizontal to the vertical components of the Green–Lagrange strain tensor $\mathbf{E} = (\mathbf{C} - \mathbf{I})/2$. In the linear elastic limit, both the logarithmic and the Green–Lagrange strains are equal to the infinitesimal strain $\boldsymbol{\epsilon}$. Then, figure 5*b* shows that for the underlying material this Poisson's ratio decreases, whereas for the cellular structures, the deformation where this ratio becomes zero or negative is the same as when the logarithmic strain was used. This is due to the fact that a component of the logarithmic strain decreases (or increases) as the corresponding Green–Lagrange strain component decreases (or increases), and may become zero or negative

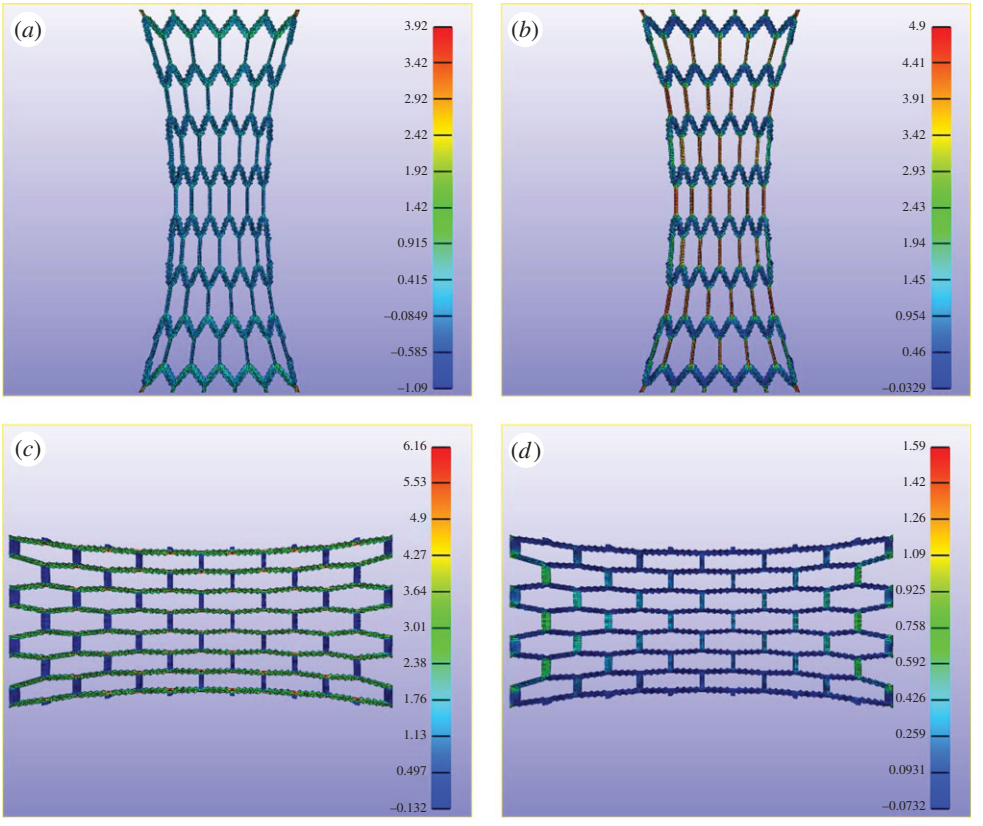

Figure 3. Extension of honeycombs with hexagonal cells, showing (*a*,*c*) horizontal and (*b*,*d*) vertical stresses owing to vertical displacement equal to 1 at the top external boundary, and to horizontal displacement equal to 1 at the right external boundary, respectively. (Online version in colour.)

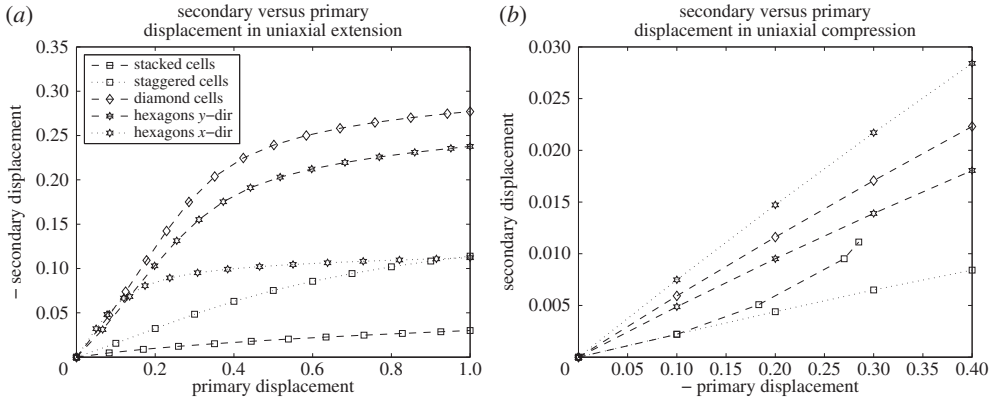

Figure 4. Secondary (transverse) versus primary (axial) displacements in uniaxial (*a*) extension and (*b*) compression.

if and only if the corresponding component of the Green–Lagrange strain also becomes zero or negative.

For a solid material deforming elastically, most of the external work stored during loading is released again when the load is removed. The *energy-absorbing capacity* of a material deforming

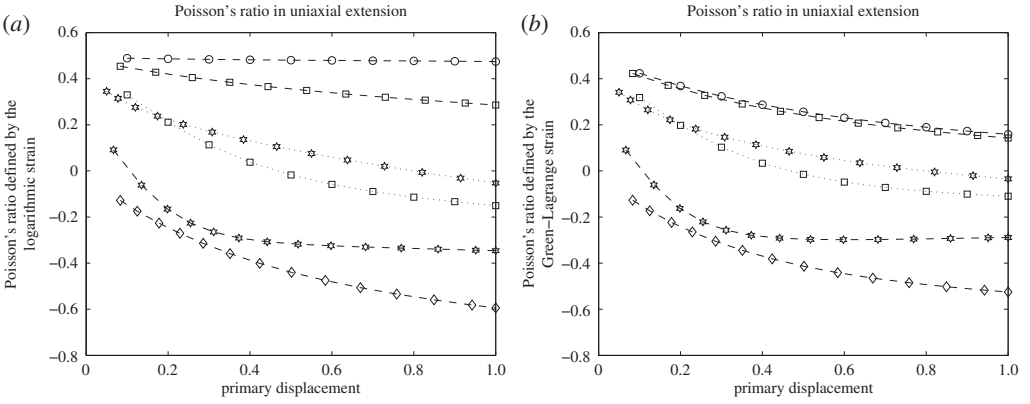

Figure 5. Poisson's ratio computed using (*a*) the logarithmic and (*b*) the Green–Lagrange strain versus the primary (axial) displacement in uniaxial extension.

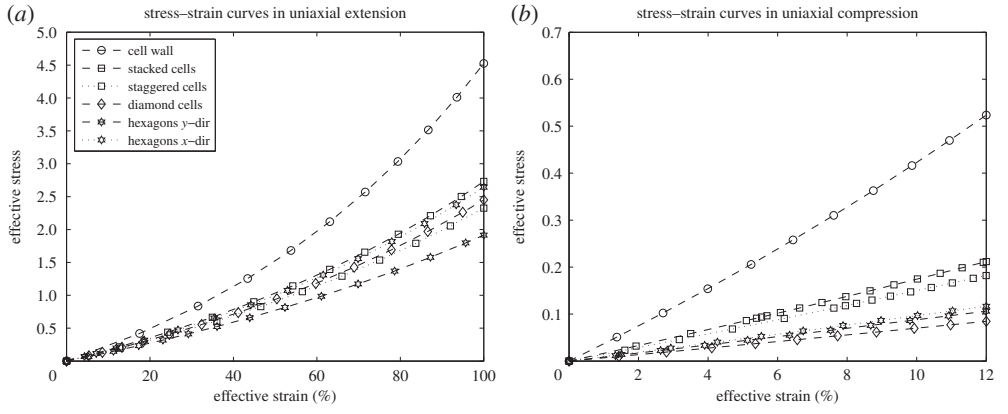

Figure 6. Stress–strain diagrams for honeycomb structures in uniaxial (*a*) extension and (*b*) compression.

to a certain strain is the work per unit volume (in the reference configuration) measured by the area under the stress–strain curve up to that strain [4, pp. 309–314]. In the stress–strain diagrams, the numerical values correspond to the average values of the Cauchy (true) stress and the logarithmic (true) strain throughout the solid part of the structure, respectively. Then, from figure 6*a*, we deduce that, up to a given stress level (assumed here below the peak stress where cell closure occurs), the honeycomb structures are more flexible and can absorb more energy than the hyperelastic material from which they were made. In addition, the structures with staggered or diamond cells absorb more energy than that with stacked cells, and the honeycomb with hexagonal cells has the capacity of absorbing more energy than those with square or diamond cells when vertically extended.

The model structures in the decreasing order of their stiffness together with their corresponding angle of the cell walls relative to the direction of the load are as follows: (i) stacked square cells extended vertically (0°); (ii) hexagonal cells extended horizontally (30°); (iii) diamond cells extended vertically (45°); (iv) hexagonal cells extended vertically (60°). For the structure with staggered cells, because the square cells eventually deform into hexagonal shapes, the stress–strain diagram is between those for the diamond cells and the hexagonal cells extended vertically when the load is sufficiently large. It has also been observed, in some woods, that the modulus of elasticity decreases with the increasing angle of the cell wall relative to the direction of the load [13, p. 83].

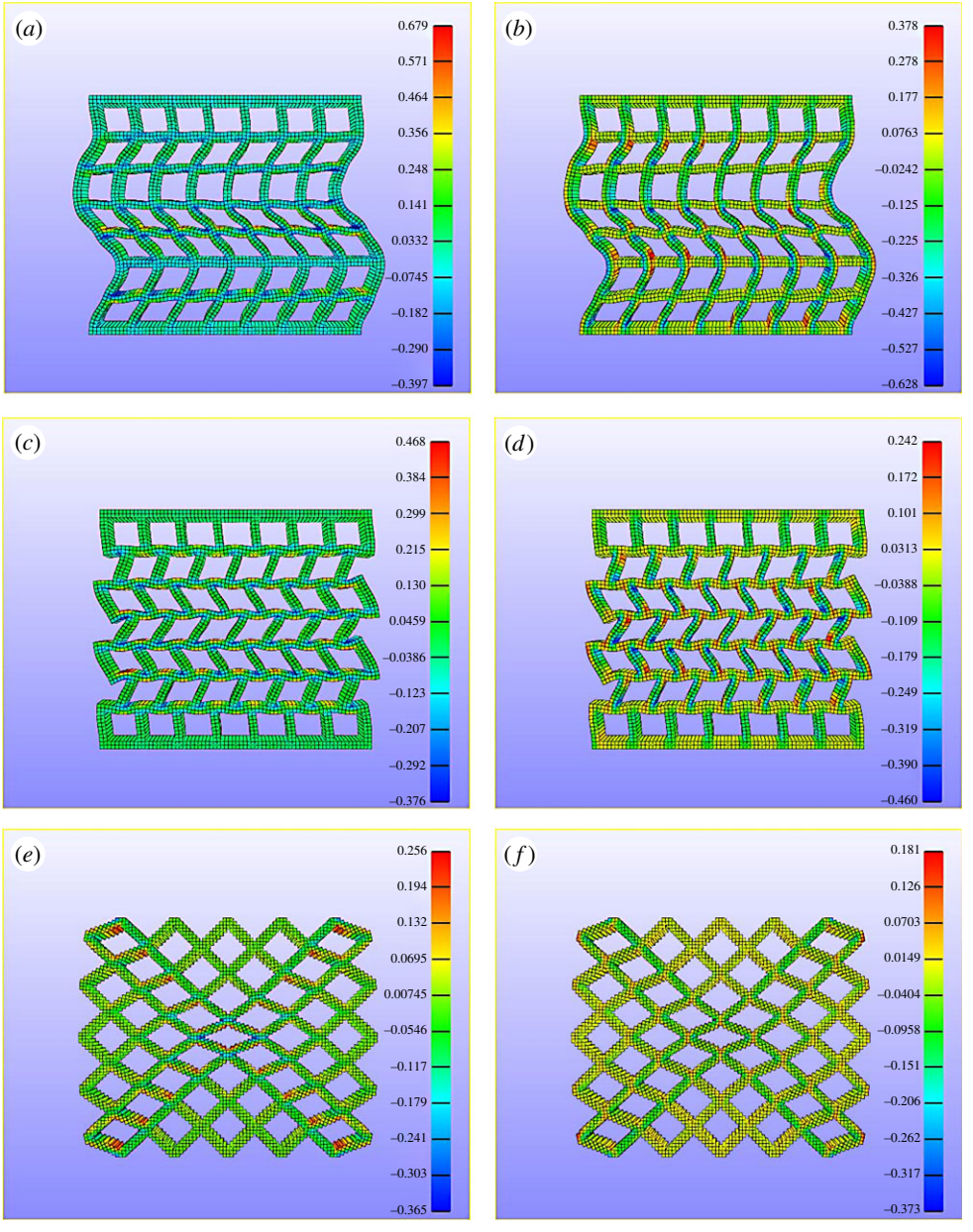

Figure 7. Vertical compression owing to vertical displacement of −0.12 at the top external boundary, showing (*a*,*c*,*e*) horizontal and (*b*,*d*,*f*) vertical stresses in honeycombs with stacked, staggered, and diamond cells, respectively. (Online version in colour.)

Under the action of *large vertical compressive forces*, the behaviour of honeycomb structures is rather different. Figures 7 and 8 show that the structures with square cells will buckle, whereas the deformation of those with diamond or hexagonal cells is symmetric with respect to the vertical axis. The corresponding horizontal and vertical displacements (up to the point where the buckling starts in the structure with staggered cells) are recorded in figure 4*b*. From these diagrams, we infer that the structures with square cells extend less than the other structures in the transverse direction, whereas the structure with hexagonal cells compresses the most.

From the diagrams in figure 9*a*, we see that the Poisson's ratio defined by the components of the logarithmic strain before the buckling begins remains positive for all the different

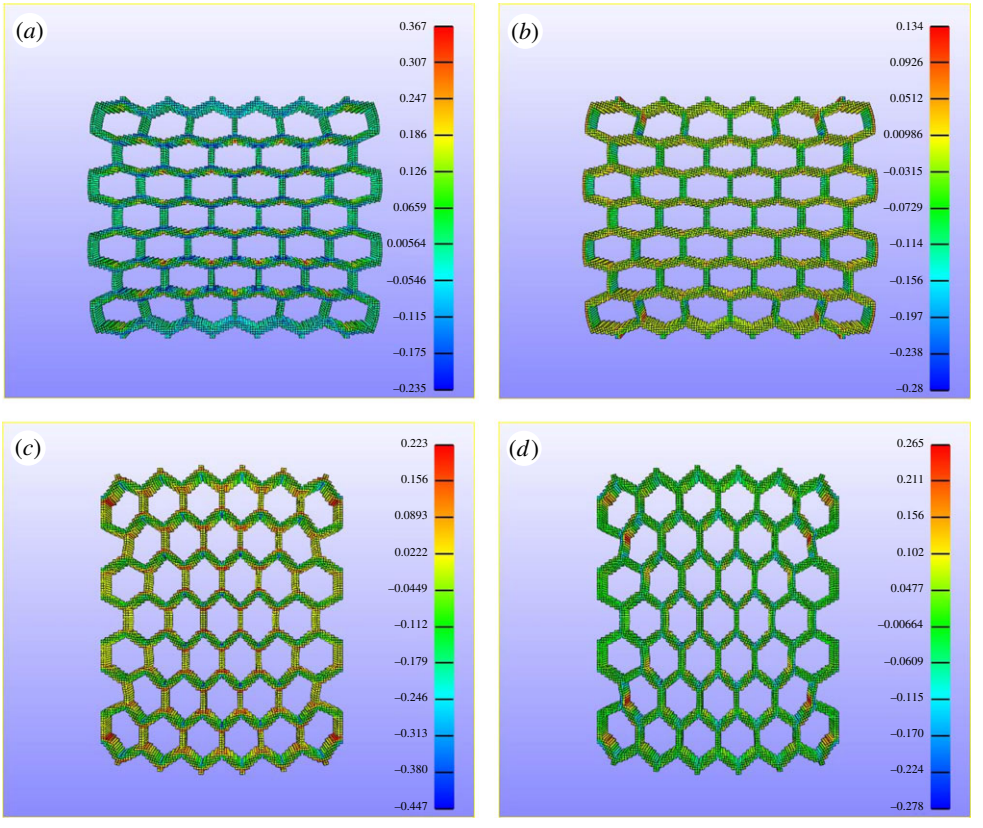

Figure 8. Compression of honeycombs with hexagonal cells, showing (*a*,*c*) horizontal and (*b*,*d*) vertical stresses owing to vertical displacement of −0.12 at the top external boundary, and to horizontal displacement of −0.12 at the right external boundary, respectively. (Online version in colour.)

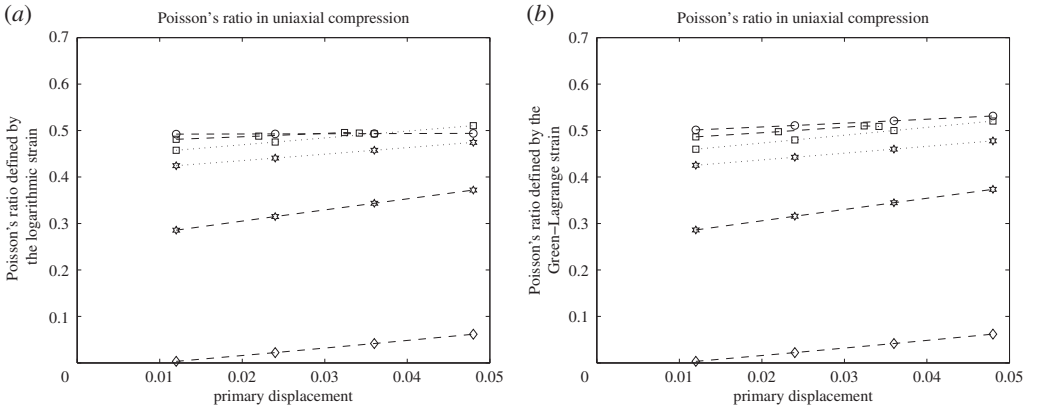

Figure 9. Poisson's ratio computed using (*a*) the logarithmic and (*b*) the Green–Lagrange strain versus the primary (axial) displacement in uniaxial compression.

structures, although its value depends strongly on the cell geometry and may become greater than 0.5 in some cases. If the components of the Green–Lagrange strain are used instead, then in figure 9*b*, an increase above the value of 0.5 is observed also for the underlying elastic material.

The stress–strain diagrams in figure 6*b* also indicate that, in compression, the diamond cells are the most flexible, followed by the hexagonal cells. This is consistent with the result obtained in the small strain regime, where hexagonal cells were found to be more flexible than square cells in general [4, pp. 159–160].

3. Inclined cell walls and the Poisson effects

Motivated by the preceding numerical results, we now focus our attention on a single oblique cell wall of a honeycomb structure which is extended or compressed vertically, and demonstrate that the Poisson effects observed in these structures are influenced by the inclination of the cell walls relative to the direction of the applied load.

We begin our analysis by assuming that, when a cellular structure is extended or compressed vertically, the displacements in the horizontal direction are much smaller than the vertical displacements, as suggested by the diagrams in figure 4. Then, under the action of the vertical force, for an inclined cell wall with the ends aligning in the vertical direction, a shear deformation develops in the same direction, whereas in the horizontal direction, the distance between the planes containing the sheared ends remains virtually unchanged (figure 10).

For the cell wall elastic material, we require the validity of the Baker–Ericksen (BE) inequalities stating that *the greater principal stress occurs in the direction of the greater principal stretch*, and of the pressure–compression (PC) inequalities stating that *each principal stress is a pressure* (*compression*) *or a tension according as the corresponding principal stretch is a contraction or an elongation* (*extension*) [7, pp. 155–159]. These inequalities are satisfied by most elastic materials.

To handle the nonlinear deformation of the elastic wall, we employ the following successive decomposition procedure (SDP):

1. We start with the simple shear (SS) deformation (3.1) everywhere in the wall.
2. Then, we allow the inclined sides of the wall to deform freely by removing the traction constraints, whereas the SS conditions at the sheared ends are maintained.

Successive decomposition procedure. The successive deformation decomposition can be formally written as follows: if $\mathbf{x}' = \boldsymbol{\chi}'(\mathbf{X}) \in \mathbb{R}^3$ describes the first deformation at step (i), and $\mathbf{x} = \boldsymbol{\chi}(\mathbf{X}) \in \mathbb{R}^3$ is the final deformation of step (ii) relative to the material configuration $\mathcal{B}_0$, then the deformation

$$\mathbf{x}'' = \boldsymbol{\chi}''(\mathbf{x}') = \boldsymbol{\chi}(\boldsymbol{\chi}'^{-1}(\mathbf{x}'))$$

maps the deformed state $\mathcal{B}'$ to the final configuration $\mathcal{B}$ (figure 11).

Let

$$\mathbf{F} = \frac{\mathrm{d}\boldsymbol{\chi}(\mathbf{X})}{\mathrm{d}\mathbf{X}}, \quad \mathbf{F}' = \frac{\mathrm{d}\boldsymbol{\chi}'(\mathbf{X})}{\mathrm{d}\mathbf{X}} \quad \text{and} \quad \mathbf{F}'' = \frac{\mathrm{d}\boldsymbol{\chi}''(\mathbf{x}')}{\mathrm{d}\mathbf{x}'}$$

be the corresponding deformation gradients, such that $\det \mathbf{F}' > 0$ and $\det \mathbf{F}'' > 0$, i.e. the mappings $\boldsymbol{\chi}'$ and $\boldsymbol{\chi}''$ are invertible and orientation preserving. Then, by the chain rule, the following compatible multiplicative decomposition holds

$$\mathbf{F} = \mathbf{F}''\mathbf{F}'.$$

Remark 3.1. The SDP exploits the fact that, under large loading conditions, the homogeneously (affine) deformed state at step (i) is potentially closer to the final configuration at step (ii) than the undeformed state and can be maintained in every homogeneous isotropic hyperelastic material under appropriate loading conditions [17,18]. Then, the (constant) stresses for this known configuration can be used to study the final 'free shape' deformation.

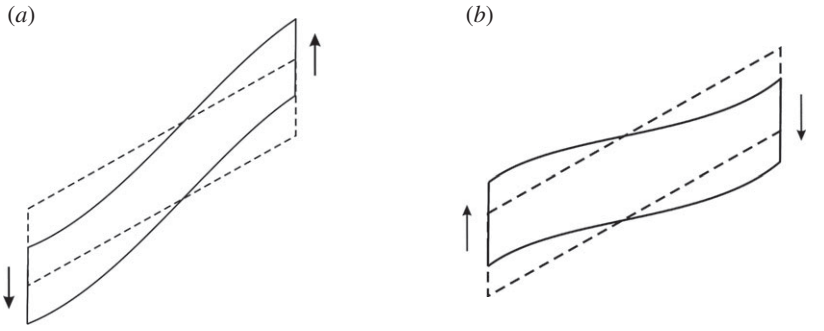

Figure 10. Inclined wall in the undeformed state (dashed line) and deformed state (solid line) owing to vertical (*a*) extension or (*b*) compression (indicated by arrows) acting at the ends.

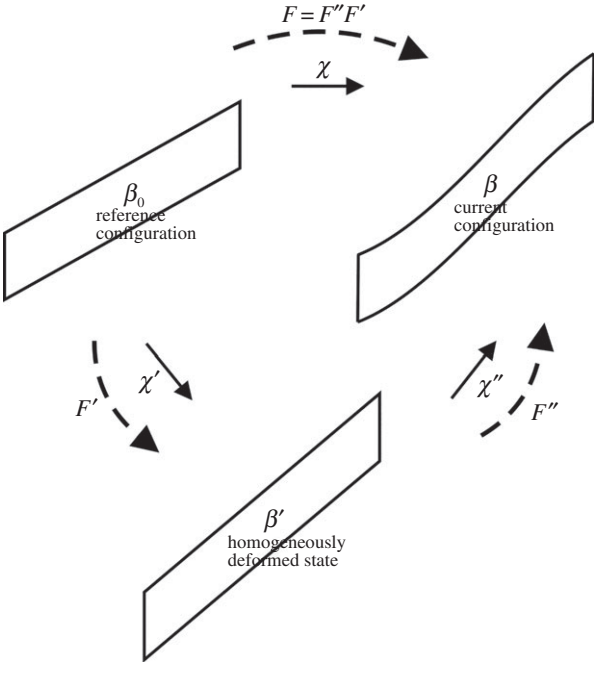

Figure 11. Schematic of the successive deformation decomposition.

When a square section of an elastic material is subjected to the SS deformation:

$$x_1 = X_1, \quad x_2 = KX_1 + X_2, \quad x_3 = X_3, \tag{3.1}$$

where $K > 0$ is constant, whereas the planes of shear are free, i.e. $\sigma_{33} = 0$, by the representation (2.2), the non-zero components of the Cauchy stress tensor are

$$\sigma_{11} = \beta_{-1}K^2, \quad \sigma_{22} = \beta_1 K^2, \quad \sigma_{12} = (\beta_1 - \beta_{-1})K.$$

Then, for the SS deformation (3.1), the principal stretches take the form

$$\lambda_1^2 = 1 + \frac{K^2 + K\sqrt{K^2+4}}{2} = \lambda^2, \quad \lambda_2^2 = 1 + \frac{K^2 - K\sqrt{K^2+4}}{2} = \lambda^{-2}, \quad \lambda_3^2 = 1, \tag{3.2}$$

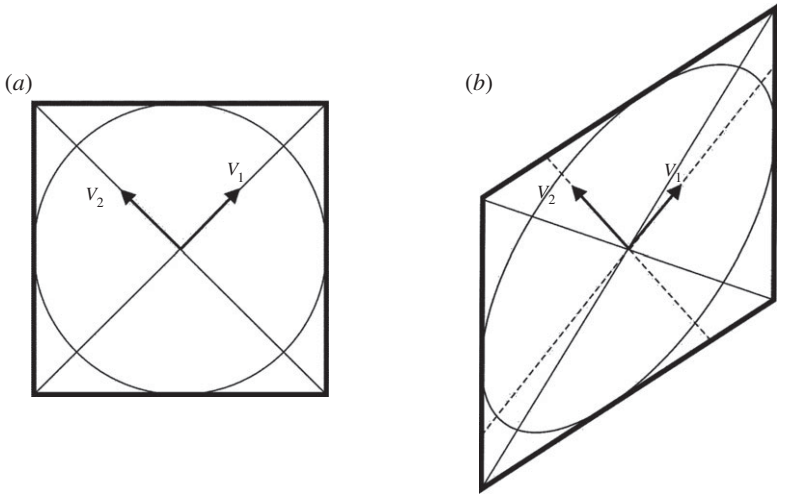

Figure 12. Square section of a material (*a*) before and (*b*) after the simple shear deformation, with arrows indicating the principal directions.

and the non-zero principal stresses are

$$\sigma_1 = \beta_1 \frac{K^2 + K\sqrt{K^2+4}}{2} + \beta_{-1} \frac{K^2 - K\sqrt{K^2+4}}{2},$$
$$\sigma_2 = \beta_1 \frac{K^2 - K\sqrt{K^2+4}}{2} + \beta_{-1} \frac{K^2 + K\sqrt{K^2+4}}{2}.$$

Let $\{\mathbf{e}_i\}_{i=1,2,3}$ denote the unit vectors in the Lagrangian directions (axes) $\{X_i\}_{i=1,2,3}$, respectively, and $\{\mathbf{v}_i\}_{i=1,2,3}$ be the unit vectors in the principal (Eulerian) directions of the SS deformation (3.1), such that $\mathbf{B}\mathbf{v}_i = \lambda_i^2 \mathbf{v}_i$, $i = 1, 2, 3$, where $\mathbf{B} = \mathbf{F}\mathbf{F}^{\mathrm{T}}$ is the left Cauchy–Green strain tensor. Explicitly, the principal directions are

$$\mathbf{v}_1 = \mathbf{e}_1 \cos\alpha + \mathbf{e}_2 \sin\alpha, \quad \mathbf{v}_2 = -\mathbf{e}_1 \sin\alpha + \mathbf{e}_2 \cos\alpha, \quad \mathbf{v}_3 = \mathbf{e}_3, \tag{3.3}$$

where

$$\tan\alpha = \frac{K + \sqrt{K^2+4}}{2}, \quad \frac{\pi}{4} \le \alpha < \frac{\pi}{2}. \tag{3.4}$$

Then

$$\mathbf{B} = \mathbf{R}\mathbf{U}^2\mathbf{R}^{\mathrm{T}}, \tag{3.5}$$

where

$$\mathbf{R} = \begin{bmatrix} \cos\alpha & -\sin\alpha & 0 \\ \sin\alpha & \cos\alpha & 0 \\ 0 & 0 & 1 \end{bmatrix} \quad \text{and} \quad \mathbf{U} = \begin{bmatrix} \lambda & 0 & 0 \\ 0 & \lambda^{-1} & 0 \\ 0 & 0 & 1 \end{bmatrix},$$

and by the polar decomposition theorem, $\mathbf{F} = \mathbf{R}\mathbf{U}$.

Geometrically, the circle inscribed in the unit square $[0,1] \times [0,1]$ deforms into an ellipse with the major axis along the principal direction $\mathbf{v}_1$ and eccentricity λ^2, and because $1 < \tan\alpha < K + 1$ for $0 < K < \infty$, the principal axes are situated between the diagonals of the undeformed and sheared square, respectively (figure 12).

In the limiting case when $K \to 0$, $\tan\alpha \to 1$, the Eulerian directions are along the diagonals of the unit square in the undeformed state, and if $K \to \infty$, then $\tan\alpha \to K + 1$, and the first principal

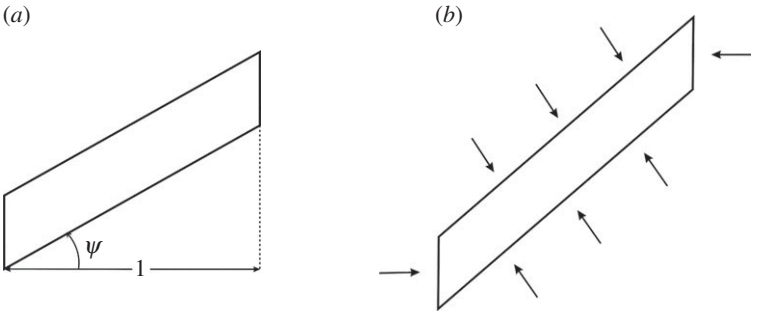

Figure 13. Inclined wall in (*a*) undeformed and (*b*) simple shear state with arrows indicating normal tractions.

direction is effectively on the longer diagonal of the deformed body. In the linear elastic limit, $K = \epsilon \ll 1$, the relative angle is $\alpha = \pi/4$.

In general

$$\sigma_1 - \sigma_3\lambda^{-2} = \beta_0(1 - \lambda^{-2}) + \beta_1(\lambda^2 - \lambda^{-2}),$$

and, when the BE inequalities are valid, the left-hand side is positive, hence the following generalized empirical inequalities may hold

$$\beta_0 \leq 0 \quad \text{and} \quad \beta_1 > 0.$$

Then, by setting $\beta_{-1} \leq 0$, we obtain that $\sigma_{11} \leq 0$, i.e. a compressive stress may be required to prevent the plane sections perpendicular to the X_1-direction from moving in the X_1-direction (this is the well-known positive Poynting effect [19,20]).

When the material is linearly elastic, the deformation generated by vertical extension at the ends is an SS with parameter $K \ll 1$. Then, the strain tensor reduces to

$$\mathbf{B} = \begin{bmatrix} 1 & K & 0 \\ K & 1 & 0 \\ 0 & 0 & 1 \end{bmatrix},$$

and the corresponding Cauchy stress takes the pure shear form

$$\boldsymbol{\sigma} = \begin{bmatrix} 0 & S & 0 \\ S & 0 & 0 \\ 0 & 0 & 0 \end{bmatrix}.$$

Thus, there is no deformation in either the horizontal or the vertical direction in this case.

We now consider an oblique cell wall which is initially inclined at an angle $\Psi \in (0, \pi/2)$ (measured anticlockwise) from the horizontal direction, and such that the distance between the (vertical) planes containing the ends of the wall is equal to one, represented graphically in figure 13*a*. If this wall is subjected to vertical extension at the ends, whereas the horizontal distance between the ends is fixed, as shown in figure 10*a*, then:

1. At the first step of the SDP, the inclined wall deforms by an SS deformation and the following result holds.

Lemma 3.2. *If the inclined wall shown in figure 13 deforms by the SS* (3.1)*, then*:

1. *On the inclined sides, the normal traction is compressive, i.e.* $\sigma_n < 0$*, while the tangential traction satisfies* $\sigma_t \leq 0$ *if* $\Psi \in (0, \pi/4)$ *and* $0 < K \leq 2/\tan(2\Psi)$*, and* $\sigma_t > 0$ *otherwise*;
2. *At the sheared ends, the normal and tangential tractions satisfy* $\sigma_n < 0$ *and* $\sigma_t > 0$.

Proof. (i) If in the undeformed (reference) state, the direction of the inclined sides is given by the vector:

$$\mathbf{D} = \begin{bmatrix} \cos\Psi \\ \sin\Psi \\ 0 \end{bmatrix},$$

then after the SS deformation, the direction of these sides becomes

$$\mathbf{d} = \mathbf{F}'\mathbf{D}.$$

In this case, on the deformed sides, the unit normal and tangent vectors are, respectively

$$\mathbf{n} = \pm \frac{1}{\sqrt{K^2\cos^2\Psi + 2K\cos\Psi\sin\Psi + 1}} \begin{bmatrix} K\cos\Psi + \sin\Psi \\ -\cos\Psi \\ 0 \end{bmatrix},$$

$$\mathbf{t} = \pm \frac{1}{\sqrt{K^2\cos^2\Psi + 2K\cos\Psi\sin\Psi + 1}} \begin{bmatrix} \cos\Psi \\ K\cos\Psi + \sin\Psi \\ 0 \end{bmatrix}.$$

Hence, the corresponding normal and shear tractions are

$$\begin{aligned} \sigma_n &= \frac{\sigma_{11}(K\cos\Psi + \sin\Psi)^2 - 2\sigma_{12}\cos\Psi(K\cos\Psi + \sin\Psi) + \sigma_{22}\cos^2\Psi}{K^2\cos^2\Psi + 2K\cos\Psi\sin\Psi + 1} \\ &= \beta_{-1}K^2 + (\beta_{-1} - \beta_1)\frac{K^2\cos^2\Psi + 2K\sin\Psi\cos\Psi}{K^2\cos^2\Psi + 2K\sin\Psi\cos\Psi + 1} \end{aligned} \tag{3.6}$$

and

$$\begin{aligned} \sigma_t &= \frac{(\sigma_{11} - \sigma_{22})\cos\Psi(K\cos\Psi + \sin\Psi) - \sigma_{12}\cos^2\Psi + \sigma_{12}(K\cos\Psi + \sin\Psi)^2}{K^2\cos^2\Psi + 2K\cos\Psi\sin\Psi + 1} \\ &= (\beta_1 - \beta_{-1})\frac{K(K\sin\Psi\cos\Psi - \cos^2\Psi + \sin^2\Psi)}{K^2\cos^2\Psi + 2K\cos\Psi\sin\Psi + 1}. \end{aligned} \tag{3.7}$$

Straightforward inspection of the relations (3.6)–(3.7) then leads to the conclusion that the normal traction is compressive, i.e. $\sigma_n < 0$, whereas for the tangential traction:

— If $\Psi \in (0, \pi/4)$, then $\sigma_t \le 0$ for all $0 < K \le 2/\tan(2\Psi)$, and $\sigma_t > 0$ for all $K > 2/\tan(2\Psi)$;
— If $\Psi \in [\pi/4, \pi/2)$, then $\sigma_t > 0$ for all $K > 0$.

In the limiting case when $\Psi \approx 0$, $\sigma_t < 0$, and if $\Psi \approx \pi/2$, then $\sigma_t > 0$.

(ii) At the sheared ends, the normal and tangential tractions are, respectively:

$$\sigma_n = \sigma_{11} < 0, \quad \sigma_t = \sigma_{12} > 0.$$

■

By lemma 3.2, both the vertical ends and the inclined sides are compressed in their respective normal directions, as indicated by the arrows in figure 13*b*. In the principal directions $\mathbf{v}_1$ and $\mathbf{v}_2$ for this deformation, the corresponding stresses in the deformed wall satisfy $\sigma_1 > 0$ and $\sigma_2 < 0$, hence by the PC inequalities, the inclined wall extends in the $\mathbf{v}_1$-direction and compresses in the $\mathbf{v}_2$-direction. This is consistent with the fact that the corresponding principal stretches satisfy $\lambda_1 = \lambda > 1$ and $\lambda_2 = 1/\lambda < 1$. By the SS deformation, the inclined wall also extends vertically. However, because during this deformation, the straight lines parallel to the horizontal and vertical axes remain straight and parallel, there is no deformation in the horizontal direction.

2. At the second step of the SDP, for the pre-deformed wall, the vertical ends remain sheared and the traction constraints on the oblique sides are removed, so these sides may deform freely. Then, on the 'free' sides, the following result holds.

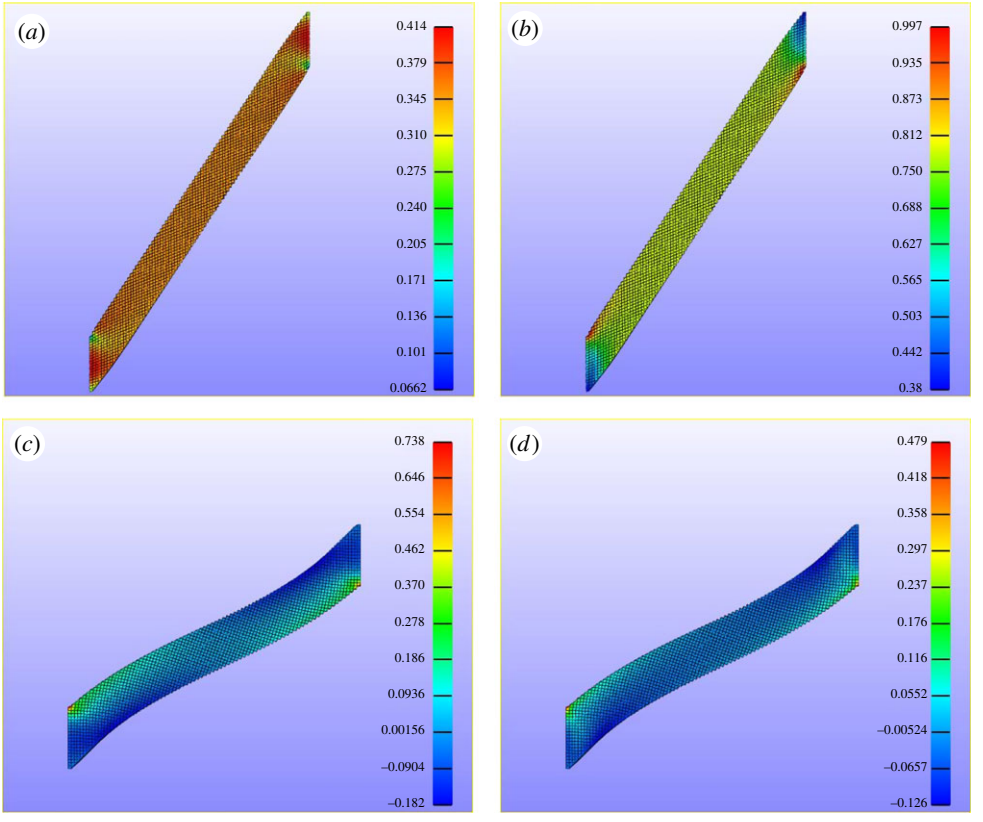

Figure 14. Inclined wall, showing (*a*,*c*) horizontal and (*b*,*d*) vertical stresses owing to vertical extension or compression at the right-end, respectively, with the left-end fixed. (Online version in colour.)

Theorem 3.3. *For the pre-deformed inclined wall, if the traction constraints at the inclined sides are removed, then these sides will expand both horizontally and vertically, creating the appearance of a negative Poisson effect in the wall which is extended vertically from its ends.*

Proof. For the pre-deformed wall at step (i), by lemma 3.2, there is a compressive normal stress $\sigma_n < 0$ on the inclined sides. Then, at step (2), assuming that the sides remain stretched longitudinally and are set free in their normal direction, the wall will expand in the directions normal to these sides. Therefore, at step (2), the inclined wall will expand in both the horizontal and the vertical direction, exhibiting an apparent negative Poisson effect in the plane defined by these directions. ■

Remark 3.4. The negative Poisson's ratio can be observed in figure 5 for the diamond cells, where all the walls are inclined relative to the loading direction, but also for the hexagonal and the staggered square cells when sufficiently deformed.

Corollary 3.5. *If the initial angle Ψ of the inclined wall is fixed and the parameter K increases, or if K is fixed and the initial angle Ψ is increased, then the (negative) Poisson's ratio in this wall decreases.*

Proof. For a fixed initial angle Ψ, when the parameter K increases, the magnitude of the normal traction (3.6) for the inclined sides at step (i) increases, hence an increasing normal force is required to set these sides free at step (ii). In addition, as K increases, the inclined wall tends to align with the vertical direction, and the normal direction to the inclined sides becomes closer to the horizontal direction. Consequently, the horizontal strain increases relative to the vertical strain, causing the (negative) Poisson's ratio to decrease. Similarly, when K is fixed and the initial

angle Ψ is increased, the normal traction (3.6) increases and its direction approaches the horizontal direction, hence the Poisson's ratio decreases. ■

Remark 3.6. In figure 5, the decrease in the Poisson's ratio as the magnitude of the vertical deformation increases can be observed in the diagram of individual structures, whereas the decrease of this ratio with respect to the initial inclination of the cell walls is accounted for by the relative position of these diagrams to each other.

When the inclined wall is subjected to vertical contraction from its ends, whereas the horizontal distance between the ends is fixed, as shown in figure 10*b*, we replace $K > 0$ by $-K < 0$ in (3.1). Then, assuming that K is sufficiently small, the deformation is homogeneous and only the first step of the SDP applies, hence there is contraction in the vertical direction, whereas in the horizontal direction, there is no deformation. Thus, the corresponding Poisson's ratio is almost zero, as observed in figure 9*b* in the case of the diamond cells, where all the walls are inclined relative to the applied force.

For numerical illustration, we consider a single oblique wall of size $1 \times 6 \times 1$ and inclined at an angle $\Psi = \pi/4$ from the horizontal, made of the same Mooney material as the honeycomb structures in §2. When a vertical displacement equal to 2 is prescribed at the right-end, whereas the left-end is fixed, the computed horizontal and vertical stresses are indicated in figures 14*a*,*b*, where the finite-element mesh is also shown. The numerical values for these stresses are all positive, and the corresponding strains are also positive, hence a negative Poisson effect is found. If a vertical displacement of -0.2 is prescribed at the right-end while the left-end is fixed, then the result is illustrated in figure 14*c*,*d*, where the buckling of the wall is observed.

4. Conclusion

In this paper, we presented a set of results regarding the Poisson effects that appear in cellular structures in large elastic deformations and analyse the physical properties that generate them. Specifically, using numerical models of honeycomb structures with hyperelastic walls and standard geometry, such as rectangular-, hexagonal- or diamond-shaped cells, we are able to uncover some of the complex mechanical processes for these structures.

We find that, when a structure is subjected to vertical tension, by computing the apparent Poisson's ratio as the negative quotient of the horizontal to the vertical components of either the logarithmic (true) or the Green–Lagrange strain generated in its elastic walls, the cell geometry may alter and a negative Poisson effect can develop owing to the nonlinear deformation of the cell walls. For these structures, the mechanical properties in compression are generally different from those in tension, and Poisson's ratios greater than 0.5 are observed in vertical compression.

Our numerical results then serve as an incentive for the mathematical mechanical analysis, whereby we establish that, when a honeycomb structure of nonlinear elastic material contains walls which are inclined relative to a uniaxial tensile load, these walls tend to expand both in the direction of the load and in the orthogonal direction, and thus an apparent negative Poisson's ratio is produced at individual cell level. Moreover, we show that this (negative) Poisson ratio decreases as the magnitude of the tensile load increases. Because, for an inclined wall made of a linearly elastic material under similar loading conditions, there is no deformation in either the horizontal or the vertical direction, similar effects in structures with linearly elastic cell walls do not occur.

We conclude that, for soft honeycomb structures with hyperelastic walls and regular geometry, exceptional mechanical properties arise from the inextricable relation between the nonlinear elastic responses and structural geometry. Moreover, although the theme here is the large range of Poisson effects exhibited by these structures, our study of the local forces which are responsible for these effects can be extended further to the case when cell collapse or more complex structures with non-empty cells are modelled.

The numerical results presented here also show that different cell shapes lead to different structural responses, with some structures being more flexible or absorbing more energy than

others under tensile or compressive loads. Although the cellular structure confers no automatic advantage under compression, its flexibility supervenes that of the material from which it was made, both in tension and in compression, and it also allows for change of shape under specific external conditions. This then leads to further changes in the material properties, which are measurable though perhaps not visible and may play a significant role in creating opportunities for new applications.

Acknowledgements. A.G. is a Wolfson/Royal Society Merit Award Holder and acknowledges support by the Marie Curie European Reintegration grant no. BKRVRG0. The support for L.A.M. by the Institute of Mathematics and its Applications (IMA) grant no. SGS10/13 is also gratefully acknowledged.

References

1. Meyers MA, Chen P-Y, Lin AY-M, Seki Y. 2008 Biological materials: structure and mechanical properties. *Prog. Mater. Sci.* **53**, 1–206. (doi:10.1016/j.pmatsci.2007.05.002)
2. Gibson LJ, Ashby MF, Harley BA. 2010 *Cellular materials in nature and medicine*. Cambridge, UK: Cambridge University Press.
3. Humphrey JD. 2003 Continuum biomechanics of soft biological tissues. Review paper. *Proc. R. Soc. Lond. A* **459**, 3–46. (doi:10.1098/rspa.2002.1060)
4. Gibson LJ, Ashby MF. 1997 *Cellular solids: structure and properties*, 2nd edn. Cambridge, UK: Cambridge University Press.
5. Weaire D, Fortes MA. 1994 Stress and strain in liquid and solid foams. *Adv. Phys.* **43**, 685–738. (doi:10.1080/00018739400101549)
6. Ogden RW. 1997 *Non-linear elastic deformations*, 2nd edn. New York, NY: Dover.
7. Truesdell C, Noll W. 2004 *The non-linear field theories of mechanics*, 3rd edn. Berlin, Germany: Springer.
8. Beatty MF, Stalnaker DO. 1986 The Poisson function of finite elasticity. *J. Appl. Math.* **53**, 807–813.
9. Baker M, Ericksen JL. 1954 Inequalities restricting the form of stress-deformation relations for isotropic elastic solids and Reiner–Rivlin fluids. *J. Washington Acad. Sci.* **44**, 33–35.
10. Marzano S. 1983 An interpretation of Baker–Ericksen inequalities in uniaxial deformation and stress. *Meccanica* **18**, 233–235. (doi:10.1007/BF02128248)
11. Beatty MF. 1987 Topics in finite elasticity: hyperelasticity of rubber, elastomers, and biological tissues: with examples. *Appl. Mech. Rev.* **40**, 1699–1734. (doi:10.1115/1.3149545)
12. Fortes MA, Nogueira MT. 1989 The Poisson effect in cork. *Mater. Sci. Eng. A* **122**, 227–232. (doi:10.1016/0921-5093(89)90634-5)
13. Dinwoodie JM. 1981 *Timber, its nature and behaviour*. New York, NY: Van Nostrand Reinhold.
14. Oden JT. 2006 *Finite elements of nonlinear continua*, 2nd edn. New York, NY: Dover.
15. Le Tallec P. 1994 Numerical methods for three-dimensional elasticity. In *Handbook of numerical analysis* (eds PG Ciarlet, JL Lions), vol. 3. Amsterdam, The Netherlands: Elsevier Sciences B.V., pp. 465–622.
16. Maas SA, Ellis BJ, Ateshian GA, Weiss JA. 2012 FEBio: finite elements for biomechanics. *J. Biomech. Eng.* **134**, 01100. (doi:10.1115/1.4005694)
17. Ericksen JL. 1955 Deformation possible in every compressible isotropic perfectly elastic materials. *J. Math. Phys.* **34**, 126–128.
18. Shield RT. 1971 Deformations possible in every compressible, isotropic, perfectly elastic material. *J. Elast.* **1**, 91–92. (doi:10.1007/BF00045703)
19. Mihai LA, Goriely A. 2011 Positive or negative Poynting effect? The role of adscititious inequalities in hyperelastic materials. *Proc. R. Soc. A* **467**, 3633–3646. (doi:10.1098/rspa.2011.0281)
20. Mihai LA, Goriely A. 2013 Numerical simulation of shear and the Poynting effects by the finite element method: an application of the generalised empirical inequalities in non-linear elasticity. *Int. J. Non-Linear Mech.* **49**, 1–14. (doi:10.1016/j.ijnonlinmec.2012.09.001)